

## Journal Pre-proof

Spatial decay of electromagnetic waves from hypervelocity impact plasmas

Raymond Lau, Nicolas Lee, Sigrid Elschot



PII: S0734-743X(24)00049-6  
DOI: <https://doi.org/10.1016/j.ijimpeng.2024.104924>  
Reference: IE 104924

To appear in: *International Journal of Impact Engineering*

Received date: 17 November 2023  
Revised date: 24 January 2024  
Accepted date: 18 February 2024

Please cite this article as: R. Lau, N. Lee and S. Elschot, Spatial decay of electromagnetic waves from hypervelocity impact plasmas. *International Journal of Impact Engineering* (2024), doi: <https://doi.org/10.1016/j.ijimpeng.2024.104924>.

This is a PDF file of an article that has undergone enhancements after acceptance, such as the addition of a cover page and metadata, and formatting for readability, but it is not yet the definitive version of record. This version will undergo additional copyediting, typesetting and review before it is published in its final form, but we are providing this version to give early visibility of the article. Please note that, during the production process, errors may be discovered which could affect the content, and all legal disclaimers that apply to the journal pertain.

© 2024 Published by Elsevier Ltd.

## 1 Highlights

### 2 **Spatial Decay of Electromagnetic Waves from Hypervelocity Impact Plasmas**

3 Raymond Lau<sup>1</sup>, Nicolas Lee, Sigrid Elschot

- 4 • Hypervelocity-impact-generated plasmas can create electromagnetic pulses (EMPs)
- 5 • The EMP waveform is asymmetric due to small fluctuations in the plasma
- 6 • The EMP frequency is proportional to the plasma frequency with a direct correlation  
7 between radiation frequency and plasma density
- 8 • The plasma produced acts as a plasma antenna with spatial decay similar to classical  
9 antenna theory

---

<sup>1</sup>Corresponding Author, email: rl49@stanford.edu

# Spatial Decay of Electromagnetic Waves from Hypervelocity Impact Plasmas

Raymond Lau<sup>1a</sup>, Nicolas Lee<sup>a</sup>, Sigrid Elschot<sup>a</sup>

<sup>a</sup>*Department of Aeronautics & Astronautics, Stanford University, 496 Lomita Mall, Stanford, 94305, CA, USA*

---

## Abstract

Due to the high kinetic energy of impactors in space, hypervelocity impacts on spacecraft can ablate spacecraft material and produce plasmas. These plasmas have been observed in ground-based experiments to produce electromagnetic pulses (EMPs) and are suspected to be a cause of spacecraft anomalies. The initial EMP that is produced after plasma formation is replicated using a 2D electromagnetic plasma simulation, consisting of a discontinuous Galerkin, particle-in-cell (DG-PIC) framework. The spontaneous formation of EMPs from an initial quasineutral plasma is consistent with previous works and show behavior similar to that of waves emitted by antennas. The EMP emits from the plasma with a frequency less than the plasma frequency associated with the point of maximum density, showing the importance of the density gradient, and the far-field region of the “plasma antenna” is estimated. From the proportionality between plasma frequency and EMP frequency, there is a direct correlation between plasma density and radiation. As the plasma density decreases, the EMP frequency decreases, which suggests that several observable phenomena, such as optical flashes, radio frequency emission, and microwave emission, all result from the same plasma-related mechanism within a single hypervelocity impact.

*Keywords:* Discontinuous Galerkin, particle-in-cell, hypervelocity impact, plasma, plasma antenna

---

## 1. Introduction

In the space environment, spacecraft are impacted by a higher flux of smaller particles, such as micrometeoroids and debris, compared to larger impactors [1, 2]. These smaller impactors have velocities typically greater than 11 km/s for naturally occurring microme-

---

<sup>1</sup>Corresponding Author, email: r149@stanford.edu  
Preprint submitted to *International Journal of Impact Engineering*

35 teoroids and 7 km/s for artificially created space debris. For micrometeoroids, this velocity  
36 corresponds to around Earth's orbital escape velocity, while for orbital debris, this lower  
37 bound is determined by the orbital velocity of debris in altitudes at the upper end of Lower  
38 Earth Orbit (LEO). Due to their high kinetic energy, these hypervelocity impacts can ablate  
39 the impactor and spacecraft surface, leading to vaporization and ionization of the material,  
40 forming a plasma. The plasmas that are produced have been linked to electrical damage  
41 on spacecraft [3]. For instance, the gyroscope on the *Olympus I* spacecraft spontaneously  
42 malfunctioned, leading to the spacecraft's failure during the Perseid meteoroid shower [4].  
43 Investigations into its failure showed no obvious signs of mechanical damage; however, the  
44 increased flux and higher velocities of micrometeoroids associated with the shower – 56 km/s  
45 on average [5] – suggest the failure may be electrical in nature and related to the plasma  
46 that was formed from a meteoroid impact. This is not an isolated event: spacecraft such as  
47 *Cassini* and *Landsat 5* among others have experienced electrical effects due to hypervelocity  
48 impacts [6].

49 Currently, the connection behind electrical damage and the plasmas from hypervelocity  
50 impacts is unknown. It has been observed in ground-based experiments that electromagnetic  
51 pulses (EMPs) are generated from the hypervelocity impacts on both the radio frequency  
52 (RF) [1, 7, 8] and microwave frequency spectra [9, 10]. This has been more frequently  
53 observed for higher velocity projectiles (*e.g.*, speeds greater than 20 km/s) in experiments  
54 utilizing electrostatic dust accelerators and explosive shaped charges [1, 7]. Furthermore,  
55 in-situ measurements on the Parker Solar Probe have measured plasma waves in the low  
56 frequency band below 75 kHz [11]. This emission is a suspected cause of electrical damage,  
57 and thus, understanding of the EMP is important in investigating all possible failure mech-  
58 anisms on spacecraft [6, 12]. These experiments look at mechanisms of EMP production  
59 and their corresponding frequencies; however, no previous studies to our knowledge analyze  
60 the radiation as it traverses through the spacecraft and its surrounding medium, which is  
61 important in understanding the associated electrical damage. In this work, we look into  
62 the how the EMP behaves as it propagates into the surrounding space. As the radiation  
63 emitted from the plasma traverses space, the power and the magnitude of the EMP will  
64 decrease. Fully understanding how this signal decays will give better insight into the design

65 and spacing between electrical components that may be susceptible to the EMPs generated.

66 We approach this problem from a computational perspective. Previous computational  
67 studies focus on the formation of plasma after impact and have been able to replicate radia-  
68 tion emission from hypervelocity impact plasmas. Islam *et al.* simulates plasma production  
69 in a non-vacuum environment (*i.e.* surrounded by a neutral fluid) by solving the compressible  
70 inviscid Navier-Stokes equations and the Saha ionization [13, 14]. However, electromagnetic  
71 effects and emission cannot be studied in their current framework as electric and magnetic  
72 fields are not explicitly modeled. On the other hand, Fletcher *et al.* first uses a smoothed  
73 particle hydrodynamics code to study plasma production in a vacuum from velocities ranging  
74 from 11 km/s to 72 km/s [15], which then acts as an initial condition for a nondimensional  
75 2D discontinuous Galerkin particle-in-cell (DG-PIC) simulation that replicates EMP genera-  
76 tion [16]. These works solve the Maxwell's equations directly, accounting for electromagnetic  
77 effects. However, only the initial set of emitted waves are simulated due to the first-order  
78 boundary conditions employed, which leads to numerical reflections off the boundary and  
79 cause nonphysical behavior in the plasma with longer simulations. We overcome this weak-  
80 ness within our newly developed high-performance 2D DG-PIC simulation by implementing  
81 perfectly matched layers (PMLs) at the computational boundary. With PMLs, we are able  
82 to absorb outgoing waves, decrease numerical reflections off the boundary, and observe a  
83 longer time history of the EMP from these plasmas than previously done in other studies.

84 Our simulations demonstrate that the plasma acts as a source of radiation – *i.e.*, a  
85 naturally occurring plasma antenna. This plasma antenna is characterized by **nonspherical**  
86 radiation with frequency that is limited by the maximum plasma frequency. Parallels are  
87 drawn between the decay rate of the radiation with what is predicted by classical antenna  
88 theory, finding a simulated far-field region of the antenna. There is an explicit correlation  
89 between radiation measured and plasma density, implying experiments can measure either  
90 quantity to get an order of magnitude estimate of the other. As a result of this correlation,  
91 this work suggests that several different phenomena, such as optical flashes, radio frequency  
92 emission, and microwave emission, all result from the same plasma-related mechanism within  
93 a single hypervelocity impact. Future work will include materials other than free space to  
94 understand how these waves propagate throughout the spacecraft and space environment

95 background, *e.g.* the ionosphere or magnetosphere, as well as other physics that have shown  
 96 to have significant effects on the physics of hypervelocity impact plasmas, *e.g.* charged dust  
 97 and non-vacuum environments [17, 18, 19, 20].

98 The paper is formatted as following. Section 2 discusses a brief overview of the numerical  
 99 model. Section 3 shows simulation results and discusses the behavior of the EMP generated,  
 100 correlating the EMP with plasma frequency and analyzing the EMP in the context of antenna  
 101 theory. Section 4 compares the results with the simulation with previously developed theory  
 102 by Close *et al.* [21] and experiments to gain insight into simulation improvements.

## 103 2. Review of the Discontinuous Galerkin Particle-in-Cell Numerical Framework

104 This section outlines the numerical framework of the DG-PIC simulation used to sim-  
 105 ulation the hypervelocity impact radiation. DG-PIC schemes are able to capture kinetic  
 106 effects in plasma, such as plasma instabilities. This model is based off of the model detailed  
 107 by Fletcher *et al.* [16], which builds off the original DG-PIC model for plasma simulations  
 108 by Jacobs and Hesthaven [22]. The following subsections detail (i) a brief summary of the  
 109 particle-in-cell (PIC) scheme, (ii) a brief summary of the discontinuous Galerkin (DG) scheme,  
 110 and (iii) an overview of the simulation setup.

### 111 2.1. Particle-in-Cell Scheme

112 In PIC schemes, charged species are modeled as discrete macroparticles, where each  
 113 macroparticle represents a large number of physical particles. For clarity, macroparticles  
 114 will henceforth be referred to as particles. Based off the particles' positions, the charge  
 115 density  $\rho_n$  and current density  $\vec{j}_n$  at each grid node  $n$  from each particle is calculated via

$$116 \quad \rho_n = \sum_{i=1}^N q_i S(|\vec{r}_i|, R), \quad (1)$$

$$117 \quad \vec{j}_n = \sum_{i=1}^N q_i \vec{v}_i S(|\vec{r}_i|, R), \quad (2)$$

118 where  $q_i$  is the charge of each particle,  $S(|\vec{r}_i|, R)$  is a shape weighting function dependent on  
 119 the distance  $\vec{r}_i$  from a node and numerical parameter  $R$  dictating the radius of influence a  
 120

121 particle has, and  $\vec{v}_i$  is the velocity of the particle. The specific shape function is the same  
 122 Gaussian-based shape used by Fletcher *et al.* [16].

123 The charge density and current density is then included as source terms for the DG  
 124 scheme, which is detailed in Section 2.2. Afterward, the DG scheme solves for the electric  
 125 and magnetic field at every grid node. Once the fields are known, the Lorentz force  $\vec{F}_i$  at  
 126 each  $i$  particle is given as

$$127 \quad \vec{F}_i = q_i \left( \vec{E} + \vec{v}_i \times \vec{B} \right), \quad (3)$$

128  
 129 where  $\vec{E}$  is the electric field and  $\vec{B}$  is the magnetic flux density – henceforth referred to as the  
 130 magnetic field. These fields are interpolated from surrounding nodes back onto each particle.  
 131 Details about the interpolation scheme are given by Fletcher *et al.* [16]. Once the force is  
 132 known, the particles are accelerated and pushed in time and space via the well-known Boris  
 133 push scheme. Currently, collisions are not modeled. Other works have found that Coulomb  
 134 collision models, when coupled with PIC models, can lead to numerical heating [23]. In  
 135 our previous computational work, although a significant mechanism in thermalization of the  
 136 plasma (whether physical or numerical), Coulomb collisions were found to not have a signif-  
 137 icant effect on the frequency of the emission [24]. **The total energy density (which correlates**  
 138 **with amplitude) was found to both increase and decrease in the presence of Coulomb col-**  
 139 **lisions, depending on the collision model used; however, this energy density change is still**  
 140 **within a factor of 1.5 compared to the collisionless simulation. Therefore, we neglect colli-**  
 141 **sions in this work, as the analysis conducted here is still applicable to collisional simulations.**  
 142 **Specifically, we expect the qualitative behavior, spatial frequencies, and quantitative decay**  
 143 **rate discussed in Section 3 to remain the same, while the nominal energy density itself may**  
 144 **vary by a factor of two.** Future work will investigate the influence of other collisions, such  
 145 as electron-impact ionization and elastic scattering.

## 146 2.2. Discontinuous Galerkin Scheme

147 DG schemes are useful because of their ability to capture discontinuous solutions between  
 148 elements, *e.g.* shocks, and model wave behavior (similar to the finite volume method) while  
 149 being able to obtain high-order accuracy solutions within each element and include complex  
 150 geometries via unstructured meshes (similar to the finite element method) [25]. We utilize

151 the DG scheme in order to model the EMP waves emitted from the plasma, but maintain the  
 152 capability of modeling complex geometries such as the crater formed after impact. Although  
 153 this work does not include crater geometry, the capabilities are implemented and will be  
 154 investigated in future works.

155 The equations governing the electrodynamics are the well-known Maxwell's equations.  
 156 Our simulations solve the purely hyperbolic Maxwell (PHM) equations. Because of the  
 157 discrete nature of the PIC scheme, there are inaccuracies in the calculation of the charge  
 158 density and current density on the field. In order to enforce charge conservation during the  
 159 simulation, the PHM equations introduce a variable  $\phi$  to explicitly couple Gauss's divergence  
 160 law with the Maxwell-Faraday and Ampere's laws [22, 26]. The 2D transverse magnetic PHM  
 161 equations in nondimensionalized form are

$$162 \quad \frac{\partial}{\partial t} \begin{bmatrix} E_x \\ E_y \\ B_z \\ \phi \end{bmatrix} + \frac{\partial}{\partial x} \begin{bmatrix} \chi\phi \\ B_z \\ E_y \\ \chi E_x \end{bmatrix} + \frac{\partial}{\partial y} \begin{bmatrix} -B_z \\ \chi\phi \\ -E_x \\ \chi E_y \end{bmatrix} = \begin{bmatrix} -j_x \\ -j_y \\ 0 \\ \chi\rho \end{bmatrix}, \quad (4)$$

163 where  $\chi$  is a numerical parameter dictating the speed at which the divergence error prop-  
 164 agates. For physically consistent simulations,  $\chi$  must be greater than unity [22]. Further  
 165 details regarding the DG scheme are detailed in [16, 22, 24].

166 Numerical reflections can form at the boundaries resulting from the truncated domain.  
 167 To prevent this and minimize numerical reflection error, we include PMLs: a set of computa-  
 168 tional cells near the boundary which dampen incoming waves. We show an explicit derivation  
 169 of the governing purely hyperbolic Maxwell's/perfectly matched layer (PHM-PML) equations  
 170 and numerical fluxes in Appendix A and Appendix B, respectively.

### 172 2.3. Simulation Setup

173 The simulation setup is shown in Figure 1(a). The impactor and target are both as-  
 174 sumed to be composed of iron, with the plasma composed of electrons and singly-charged  
 175 positive iron ions. The mesh is more refined near the plasma and point of impact. The  
 176 total simulation domain is  $\vec{x} \in [-10.0, 10.0] \times [-3.5, 30.5] \mu\text{m}$ . The PML spans  $3.5 \mu\text{m}$

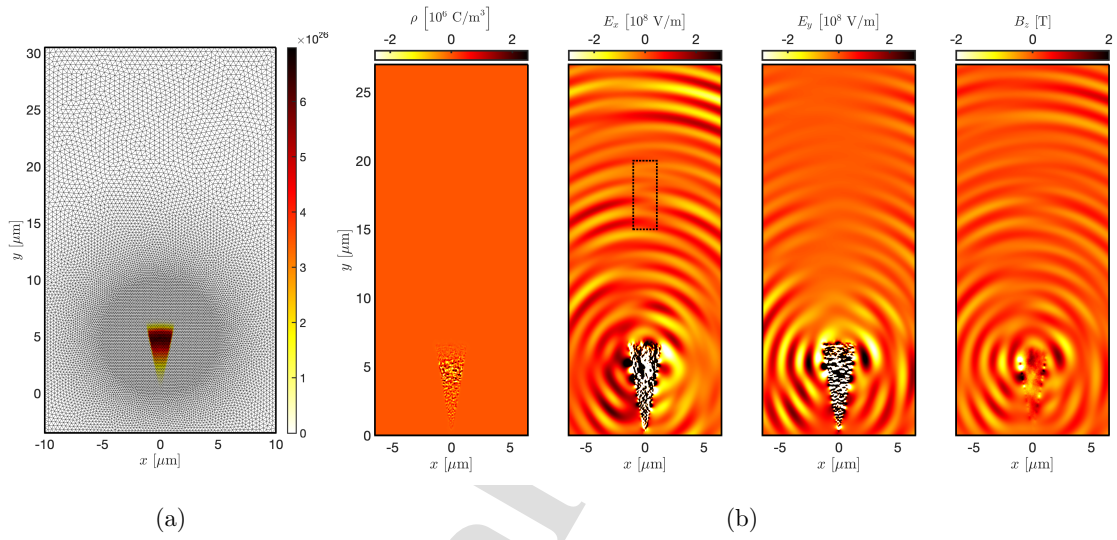


Figure 1: (a) Unstructured mesh with an initial distribution of the plasma density  $n_e$  [ $\text{m}^{-3}$ ]. This initial distribution is based off of simplified results of plasma formation caused by hypervelocity impacts from Fletcher *et al.* for a 1 ng, 20 km/s iron impactor [15]. (b) Charge density  $\rho$ , electric fields  $E_x$  and  $E_y$ , and magnetic field  $B_z$  at time  $t = 0.1 \text{ ps}$ . The dotted black box highlights a region where the EMP is not perfectly circular and a forking pattern appears.

177 on each side. Therefore, the rest of the results shown will be for the inner subdomain  
 178  $\vec{x} \in [-6.5, 6.5] \times [0, 27.0] \mu\text{m}$ .

179 Note that the plasma density is concentrated at a distance of  $4.95 \mu\text{m}$  from the impact  
 180 site; this will be shown to be approximately where the center of the EMP is generated from  
 181 rather than the impact site at  $\vec{x} = [0, 0]$ . Surrounding the plasma is a free space vacuum;  
 182 future work will include the effect of crater geometry and the effect of the electromagnetic  
 183 fields reflecting off the spacecraft. The simulation uses 24,250 fourth order elements with  
 184 characteristic length of  $0.075 \mu\text{m}$  for the most refined region and a characteristic length of  
 185  $0.225 \mu\text{m}$  for the most coarse region. The simulation results were repeated for a uniform  
 186 grid resolution of  $0.15 \mu\text{m}$  to determine the numerical errors in the nonuniform grid, which  
 187 resulted in no noticeable deviation in the results. Although the characteristic length of each  
 188 element is larger than the corresponding Debye length of the plasma ( $0.41 \text{ nm}$ ), the error is  
 189 mitigated due to the high-order nature of the DG method and current interpolation. The  
 190 simulation uses a total of 2,000,000 particles. In region populated with particles, there is an  
 191 average of 1500 particles per cell. The plasma is initialized with a temperature of 2 eV based  
 192 off of experimental measurements and plasma production simulations for a 1 ng, 20 km/s  
 193 iron impactor [8, 15]. The plasma bulk velocity is also initialized with a velocity of 20 km/s  
 194 away from the impact site; however, this velocity is over an order of magnitude slower than  
 195 the thermal velocity of the plasma and four orders of magnitude slow than the characteristic  
 196 speed of the radiation (*i.e.*, the speed of light in vacuum). Therefore, in practicality, this  
 197 bulk velocity has no effect on the radiation observed in our simulation time scales. The  
 198 simulation was conducted over a total duration of approximately 0.4 ps with a time step of  
 199 11 attoseconds resulting from the strict stability requirements of the DG-PIC model. We set  
 200 the numerical parameter  $\chi = 3$  to properly dissipate numerical waves from the divergence  
 201 cleaning error. Currently, we neglect the effects of background electric and magnetic fields,  
 202 such as those from spacecraft charging or Earth's magnetic field. Although these effects  
 203 are suspected to be significant, we wish to isolate the fundamental mechanism of radiation  
 204 production in hypervelocity impacts and opt for a simpler setup without static fields. In  
 205 future studies we will include these effects to analyze how the presence of such fields differ  
 206 from this work.

207 Our simulations are developed within an in-house code at the Space Environment and  
 208 Satellite Systems Laboratory within C++ and parallelized using Messaging Passing Interface  
 209 (MPI). The mesh is created from an open-source MATLAB script [27] with corresponding  
 210 DG matrices calculated via supplemental code provided by Hesthaven and Warburton [25].  
 211 The total wall time for the simulation was approximately 4 days over 128 processors.

### 212 3. Simulation Results and Analysis

213 Figure 1(b) shows the EMP emitted from the plasma at time  $t = 0.1$  ps. The magnitude of  
 214 the electric field is much larger in the conical plasma compared to the surrounding vacuum  
 215 region; this is attributed to the electrostatic ambipolar electric fields within the plasma  
 216 being the main governing force in maintaining a quasineutral plasma, while the EMP in  
 217 the vacuum region is electromagnetic. The amplitude of the electrostatic waves within the  
 218 plasma is approximately two orders of magnitude larger compared to the amplitude of the  
 219 electromagnetic radiation. Since the energy density is proportional to the amplitude of the  
 220 waves squared, this shows that approximately 0.01% of the electrostatic energy is converted  
 221 into electromagnetic radiation. The EMP is transverse electromagnetic, which can be seen  
 222 most easily along the line  $x = 0$ . There is an electric field in the  $x$  direction ( $E_x$ ) and a  
 223 magnetic field in the  $z$  direction ( $B_z$ ) propagating in the  $y$  direction, while  $E_y$  is much smaller  
 224 along this line relative to the surrounding regions. This shows that electromagnetic fields  
 225 only propagate perpendicular to the direction the fields are acting in. The fields radiate  
 226 around a center at approximately  $\vec{x} = [0, 4.75] \mu\text{m}$ , which coincides with the largest plasma  
 227 density. The EMP generated is not perfectly circular around this center. This can most  
 228 easily be seen in the plot of  $E_x$  around the region  $y \in [15, 20] \mu\text{m}$  along  $x = 0$ , as denoted by  
 229 the dotted black box in Figure 1(b). A forking pattern appears, which is suspected to be an  
 230 artifact of the EMP coupled with the electrostatic oscillations within the plasma. Although  
 231 this specific pattern appears along  $x = 0$ , this is not always the case, and forking patterns  
 232 are apparent in several locations throughout the simulation. Furthermore, the radiation  
 233 emitted is clearly asymmetric along  $x = 0$ , despite a quasi-symmetric initial plasma. Quasi-  
 234 symmetric in this context refers to the plasma density, which when averaged, is symmetric  
 235 about  $x = 0$ , however, local differences in symmetry due to the random initialization of

236 particle positions or thermal fluctuations in the velocities create minor asymmetries within  
 237 the plasma. This shows slight perturbations in the initial plasma can lead to significant  
 238 asymmetric radiation effects outside of the plasma.

239 Figure 2 shows the magnetic field time histories for seventeen virtual probes located  
 240 throughout the computational domain. Virtual probes were implemented in order to output  
 241 values of the electric and magnetic field at every time step, as it is computationally expensive  
 242 and impractical to output field values for every single computational node. These seventeen  
 243 probes were chosen to be positioned at three radii from the center of the radiation: near the  
 244 plasma at a radius of  $r = 2.5 \mu m$  (indicated by the blue circles), farther from the plasma at  
 245  $r = 10.0 \mu m$  (indicated by the red circles), and near the edge of the computational domain  
 246 before the PML at  $r = 21.9 \mu m$  (indicated by the green circles). These probes were placed  
 247 along rays at seven different angles  $\theta$  that vary from  $-40^\circ$  to  $40^\circ$ , where  $\theta$  is measured with  
 248 respect to the vertical  $x = 0$  line. The locations of these probes are shown in the bottom  
 249 center of Figure 2, with the various time histories of the probes surrounding it. Due to  
 250 the nature of the unstructured mesh, nodes may not align exactly at the intersection of  
 251 these radii and rays, and thus the closest neighboring node is chosen instead. The time is  
 252 normalized by the maximum electron plasma frequency  $\omega_{p,0}$  in Hz. In radians per second,  
 253 the maximum plasma frequency is

$$254 \quad \omega_{p,0} = \sqrt{\frac{n_{e,0}e^2}{m_e\epsilon_0}}, \quad (5)$$

255 where  $n_{e,0}$  is the maximum electron density (plasma density),  $e$  is the elementary charge,  $m_e$   
 256 is the electron mass, and  $\epsilon_0$  is the permittivity of free space. In our simulations, the maximum  
 257 plasma density corresponds to a plasma frequency of 230 THz. The total simulation spans  
 258 approximately  $90\omega_{p,0}$ .

259 The data shown in Figure 2 is the result of post-processing to better convey the wave  
 260 decay of the radiation. The beginning of the time history is truncated to filter the initial  
 261 numerical waves that propagate due to the divergence cleaning error. The time histories  
 262 of each ray are shifted by the propagation speed of light in vacuum,  $c_0 = 2.998 \times 10^8$  m/s  
 263 to align the local minima and maxima of the signals. This post-processing of the data is  
 264 illustrated in Figure 3. This aligns the peaks of the waves, as expected, and also illustrates

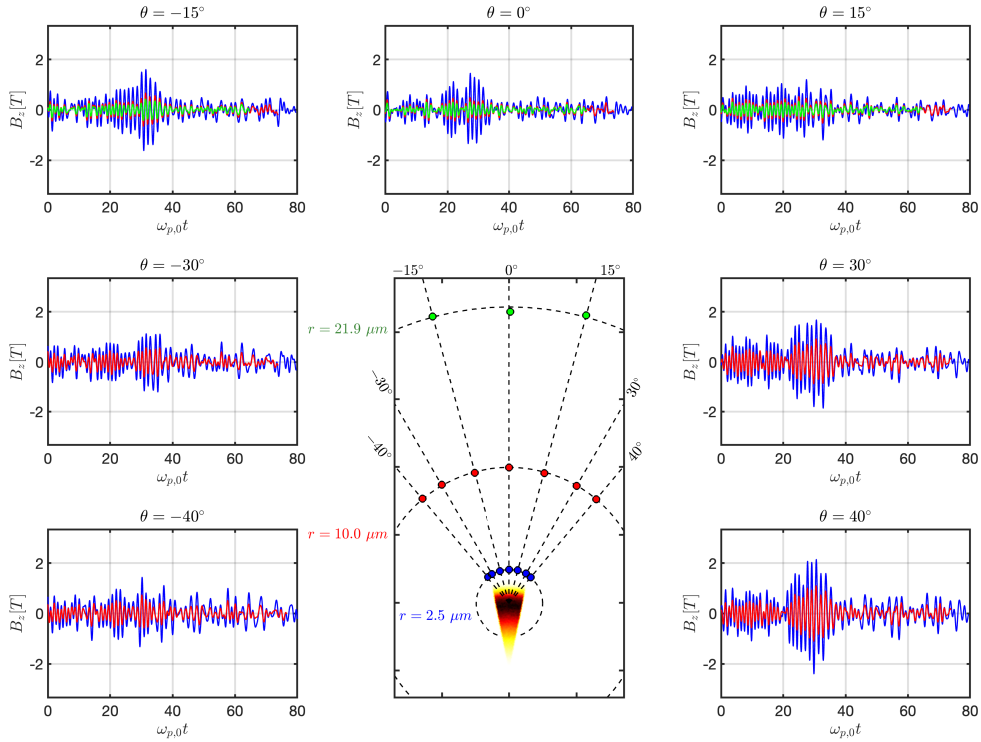


Figure 2: Time history of various probes along radii of  $r = [2.5, 10.0, 21.9] \mu\text{m}$  and along rays corresponding to  $\theta \in [-40^\circ, 40^\circ]$ . The central figure shows the locations of the various probes while the surrounding plots show the time-shifted waveform of the magnetic field  $B_z$ . The time axis is normalized by the maximum plasma frequency in Hz,  $\omega_{p,0}$ .

265 the decay in amplitude. Before the EMP reaches the outer probes, there are no fluctuations  
 266 as this region is initialized as free space.

267 Each ray shows similar behavior; the electromagnetic radiation maintains a constant  
 268 waveform but decreases in amplitude as it traverses free space. Likewise, the asymmetries  
 269 discussed previously are clearly depicted. For instance, for the probes along  $\theta \pm 40^\circ$  depict  
 270 very different behavior, with a relatively constant amplitude waveform along  $\theta = -40^\circ$  while  
 271 the signals along  $\theta = 40^\circ$  contain a large pulse. In all seven probes, there a clear pulse  
 272 that is larger than the rest of the time history. This is most clearly defined near  $\omega_{p,0}t = 30$   
 273 for  $\theta = 40^\circ$ . It is currently unknown where this specific pulse originates from. Our initial

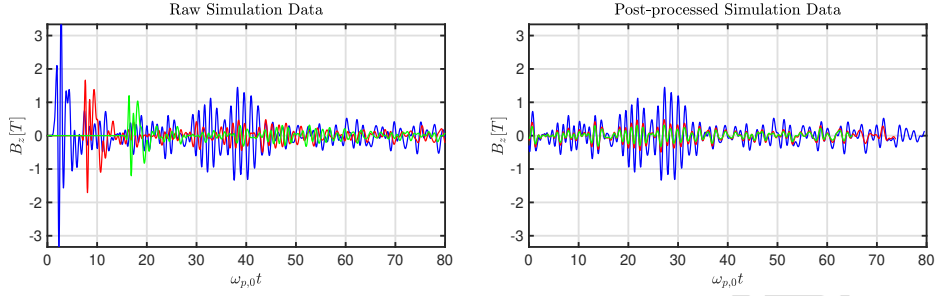


Figure 3: Example of post-processing on raw simulation data. The initial large, numerical waves due to the divergence cleaning error is truncated and the rest of the simulation data is shifted in time according to the time delay by waves traveling at the speed of light.

274 hypothesis is this pulse relates to a resonant wave mode in the conical plasma region that is  
 275 dependent on the length scale of the plasma, but further investigation will be required.

276 Figure 4 shows the power spectra of the signals measured at the seventeen probes. Asym-  
 277 metries can be seen by comparing power spectra between probes that are symmetric about  
 278  $x = 0$ , which aligns with qualitatively with what is seen in Figure 1(b), where there is no  
 279 clear single circular signal propagating in all directions. Notably, the most prominent signals  
 280 for all cases occur at a frequency  $\omega$  in between  $\omega_{p,0}/2$  and  $\omega_{p,0}$ , which corresponds to wave-  
 281 lengths  $\lambda$  ranging from 1-3  $\mu\text{m}$ . Moreover, there is effectively no prominent signal greater  
 282 than  $\omega_{p,0}$ , meaning that the frequency of the radiation is limited by the maximum plasma fre-  
 283 quency, with only prominent signals corresponding to those less than the maximum plasma  
 284 frequency. This is a counterintuitive result. The dispersion relation for an ordinary wave  
 285 traveling in a uniform plasma is

$$286 \quad \omega^2 = c_0^2 k^2 + \omega_{p,0}^2, \quad (6)$$

287 where  $\omega$  is the frequency of the wave and  $k$  is the wavenumber. This has a corresponding  
 288 frequency cutoff of  $\omega = \omega_{p,0}$ , which means electromagnetic waves propagating in the plasma  
 289 have a frequency at a minimum of the plasma frequency. In other words, the radiation  
 290 emitted from the plasma should have frequencies  $\omega \geq \omega_{p,0}$ . This discrepancy can be explained  
 291 as a result of the plasma gradient. Figure 4 has frequencies normalized by the maximum  
 292 plasma frequency. However, as the plasma density decreases, the local plasma frequency

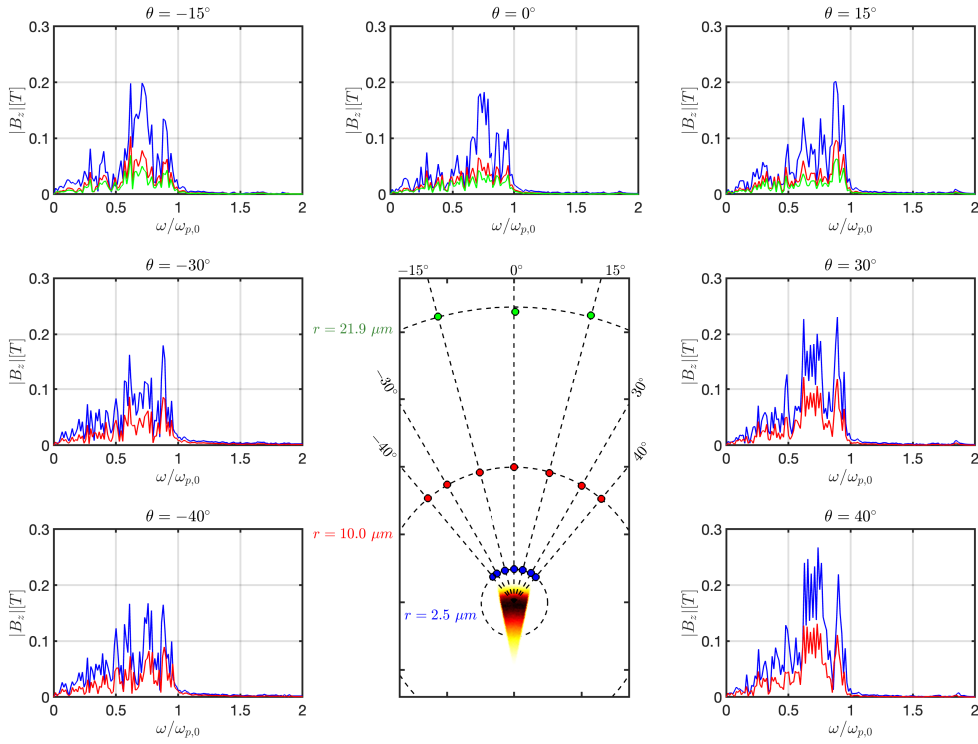


Figure 4: Power spectra for  $B_z$  of various probes along radii of  $r = [2.5, 10.0, 21.9] \mu\text{m}$  and along rays corresponding to  $\theta \in [-40^\circ, 40^\circ]$ . Most notably, all waves have signals most prominently in between  $\omega_{p,0}/2$  and  $\omega_{p,0}$  with negligible signals greater than  $\omega_{p,0}$ .

293 decreases. At the edge of the plasma, the local dispersion relation is

$$294 \quad \omega_{\text{edge}}^2 = c_0^2 k_{\text{edge}}^2 + \omega_{p,\text{edge}}^2, \quad (7)$$

295 Once an electromagnetic wave reaches the edge of the plasma to propagate in free space, the  
 296 edge plasma has a lower frequency  $\omega_{p,\text{edge}} < \omega_{p,0}$ , explaining why signals with frequencies  
 297 lower than  $\omega_{p,0}$  can propagate. Furthermore, it has been shown that electrostatic wave  
 298 modes such as electron plasma waves can convert into electromagnetic wave modes through  
 299 a density gradient [28, 29]. Our simulation setup contains a gradual density gradient where  
 300 the plasma density decreases from  $n_e = 6.5 \times 10^{26} \text{ 1/m}^3$  to approximately  $n_e = 1 \times 10^{24} \text{ 1/m}^3$   
 301 at the plasma edge followed by a sharp discontinuity that instantly decreases to zero due  
 302 to the discrete nature of the DG-PIC scheme. Theoretical studies discussing this coupling  
 303 of electrostatic and electromagnetic waves, particularly in the presence of density gradients  
 304 and discontinuities, is a complex topic deserving of its own specialized treatment and will  
 305 be presented in a future study for hypervelocity impact plasmas.

### 306 3.1. Simulation Wave Decay

307 From these results, we are interested in the attenuation, or weakening, of the EMPs  
 308 amplitude as a function of distance and time. The decay rate coefficient,  $\alpha$ , can then be  
 309 estimated from

$$310 \quad \frac{B_{z,b}}{B_{z,a}} = \left( \frac{r_b}{r_a} \right)^\alpha, \quad (8)$$

311 where  $r$  is a distance from the center of a source, and the subscripts  $a$  and  $b$  denote the  
 312 values at two different locations. We use  $B_z$  to calculate purely the electromagnetic decay  
 313 and ignore any contributions of electrostatic effects in the electric field. The simulation decay  
 314 rate is calculated by taking each of the signals from the power spectra in Figure 4, calculating  
 315 each signal's decay rate, and averaging all the rates. Table 1 summarizes the values of  $\alpha$ .  
 316 For the probes closest to the plasma, the decay rate is on average  $\alpha = -0.5568$  while the  
 317 decay rate is  $\alpha = -0.5041$  for probes farther away. As the radiation traverses free space the  
 318 spatial decay rate magnitude decreases. These values differ from the value of  $\alpha = 0.73$  that  
 319 Fletcher *et al.* reports [16]. There are several explanations for this discrepancy. Because of  
 320 the lack of the PML boundary, Fletcher *et al.* performs the analysis on the initial waves that

Table 1: Simulated decay rate  $\alpha$ 

Probe Radii Compared	$\theta$	$\alpha$	Average
$r = 2.5 \mu\text{m}$ and $r = 10.0 \mu\text{m}$	$-40^\circ$	-0.5662	-0.5568
	$-15^\circ$	-0.5975	
	$0^\circ$	-0.5507	
	$15^\circ$	-0.5572	
	$30^\circ$	-0.5496	
	$40^\circ$	-0.5109	
$r = 2.5 \mu\text{m}$ and $r = 21.9 \mu\text{m}$	$-15^\circ$	-0.5629	-0.5452
	$0^\circ$	-0.5293	
	$15^\circ$	-0.5435	
$r = 10.0 \mu\text{m}$ and $r = 21.9 \mu\text{m}$	$-15^\circ$	-0.5081	-0.5041
	$0^\circ$	-0.4905	
	$15^\circ$	-0.5200	

321 emit from the plasma, before the waves reach the boundary to avoid numerical reflections.  
322 These waves may decay more quickly due to the divergence cleaning error associated with  
323 the PHM equations. Moreover, they do not specify where in the computational domain the  
324 spatial averaging takes place. On the other hand, we analyze the spatial decay over a much  
325 longer time history than Fletcher *et al.* due to the PML capabilities while filtering out the  
326 initial numerical waves. Finally, we found the decay rate is higher near the plasma compared  
327 to farther regions, thus if Fletcher *et al.* conducted their analysis closer to the plasma, the  
328 decay rates could be much larger.

### 329 3.2. Naturally Occurring Plasma Antennas

330 The behavior of this EMP is similar to the behavior exhibited by antennas, *i.e.*, the hy-  
331 pervelocity impact plasma acts as a “naturally occurring plasma antenna.” Artificial plasma  
332 antennas are a subject of interest due to certain attractive characteristics compared to con-  
333 ventional antennas, such as their stealth features and controllability [30, 31]. Artificial  
334 plasma antennas are designed to emit radiation within the RF band, which is consistent

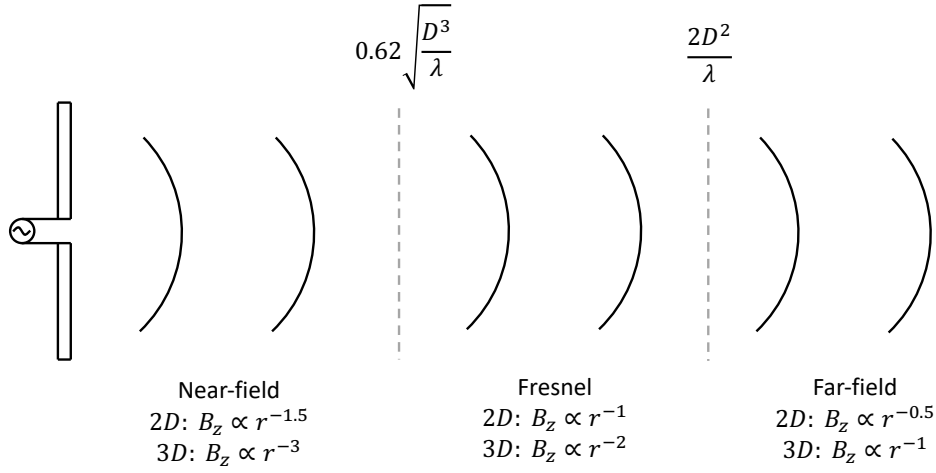


Figure 5: Radiation regions of a classical antenna

335 with the frequencies observed in experiments. Studying the behavior of the waves produced  
 336 by the naturally occurring plasma antenna in hypervelocity impact plasmas also provides  
 337 the unexpected benefit of possibly providing insight into plasma antenna design for future  
 338 works.

339 Waves closer to the antenna (or in this case, the plasma source) show larger decay com-  
 340 pared to the far-field region. In particular, the wave decay closer to the plasma is similar  
 341 to that of the near-field and Fresnel regions of an antenna, where the amplitude of a 2D  
 342 wave from an antenna is proportional to  $r^{-1.5}$  in the near-field region,  $r^{-1}$  in the Fresnel  
 343 region, and  $r^{-0.5}$  in the far-field region (or  $r^{-3}$ ,  $r^{-2}$ , and  $r^{-1}$  for a 3D wave, respectively),  
 344 as illustrated in Figure 5. The simulated average decay rate is  $\alpha = -0.5041$  for the probes  
 345 between  $r = 10.0 \mu\text{m}$  and  $r = 21.9 \mu\text{m}$ . This shows great agreement with the theoretical  
 346 decay rate for the far-field region of a 2D wave  $\alpha_{\text{theo}} = -0.5$ . The wave being 2D as opposed  
 347 to 3D is expected as the results come from a 2D electromagnetic PIC simulation. From this,  
 348 we deduce that the nodes that lie within this region are within the far-field region of the  
 349 plasma antenna.

350 For waves in the far-field region of antennas, the magnitude of the electric field and the  
 351 magnitude of the magnetic field are related via the impedance of free space  $Z_0 = \mu_0 c_0 =$

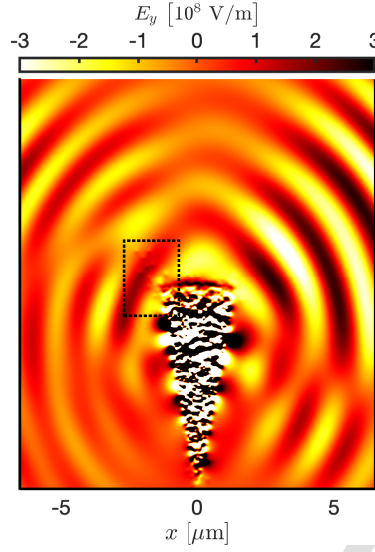


Figure 6: Electric field  $E_y$  at a time of  $t = 0.2$  ps. The region of runaway electrons is shown in the dotted box.

352  $|\vec{E}|/|\vec{H}|$ , which is the ratio of the electric field and magnetic field strength  $\vec{H} = \vec{B}/\mu_0$ , where  
 353  $\mu_0$  is the permeability of free space. From this relation, the electric field and magnetic flux  
 354 density are related simply as

$$355 \quad |\vec{E}| = |c_0 \vec{B}|. \quad (9)$$

356 Figure 7 compares these two values for the entire time history along the ray corresponding  
 357 to  $\theta = 0^\circ$ . The probes in order from closest to the plasma to farthest from the plasma will  
 358 be referred to as Probes 1, 2, and 3, respectively. The discrepancy between  $|\vec{E}|$  and  $|c_0 \vec{B}|$  in  
 359 Probe 1 is significant, supporting the claim that Probe 1 does not lie in the far-field region.  
 360 In Probes 2 and 3, there is great agreement in the value of  $|\vec{E}|$  and  $|c_0 \vec{B}|$ , particularly at the  
 361 beginning of the simulation. Probe 3 maintains the greatest agreement throughout while  
 362 Probe 2 shows larger disagreement. This is most evident in the latter half of the simulation.  
 363 This is suspected to be a result of runaway electrons; electrons with exceptionally large speed  
 364 (such as  $0.1c_0$ ) are able to travel a few microns during the simulation length, leaving the  
 365 plasma domain. These individual runaway electrons can contribute to larger electric fields at  
 366 Probe 2, changing the boundary of the far-field region. **These electrons have been observed**  
 367 **in our simulation and are evidenced by the electric field in Figure 6.**

368 As depicted in Figure 5, the general criterion for determining the boundaries of the  
 369 Fresnel region is

$$370 \quad 0.62\sqrt{\frac{D^3}{\lambda}} < r < \frac{2D^2}{\lambda}, \quad (10)$$

371 where  $D$  is the largest length of the antenna, or in this case the hypervelocity impact plasma.  
 372 Distances smaller than the lower bound define the near-field region, while distances larger  
 373 than the upper bound define the far-field region. Substituting a characteristic length of  
 374 the plasma  $D = 7 \mu\text{m}$  and a representative wavelength of  $\lambda = 1.5 \mu\text{m}$ , the lower bound is  
 375 approximately  $9.4 \mu\text{m}$ , while the upper bound (also known as the Fraunhofer distance) is  
 376 approximately  $65 \mu\text{m}$ . This suggests that Probe 1 should lie in the near-field region, while  
 377 Probes 2 and 3 should lie Fresnel region. This contradicts the results of the simulation. It  
 378 should be noted that this criterion is in general for manmade antennas, and thus applying  
 379 this criterion for a naturally made plasma may be invalid. Furthermore, this criterion may  
 380 only be applicable for 3D waves and the boundaries of each region may differ for a 2D  
 381 simulation.

382 To summarize, there are numerous parallels between the simulation results and classical  
 383 antenna theory. We have deduced that the plasma antenna radiation amplitude is a 2D  
 384 electromagnetic wave that decays proportional to near  $r^{-0.5}$ , which has great agreement with  
 385 the far-field region of a classical antenna. Furthermore, both the simulation and classical  
 386 antenna have an impedance equal to the impedance of free space, which is a characteristic of  
 387 the far-field region of classical antennas. The only discrepancy that we have noticed is where  
 388 the boundaries of the near-field, Fresnel, and far-field regions lie. Despite this, the number of  
 389 parallels significantly outnumber the discrepancies, suggesting that classical antenna theory  
 390 can be slightly modified to apply for this application.

#### 391 4. Comparison with Existing Literature

392 This section compares the characteristics of the EMP with what is predicted by previously  
 393 developed theory [21] and experiments [1, 8]. The following subsections describe (i) a short  
 394 review of the theory, (ii) comparison of the simulations with theory, and (iii) comparisons  
 395 with experiments.

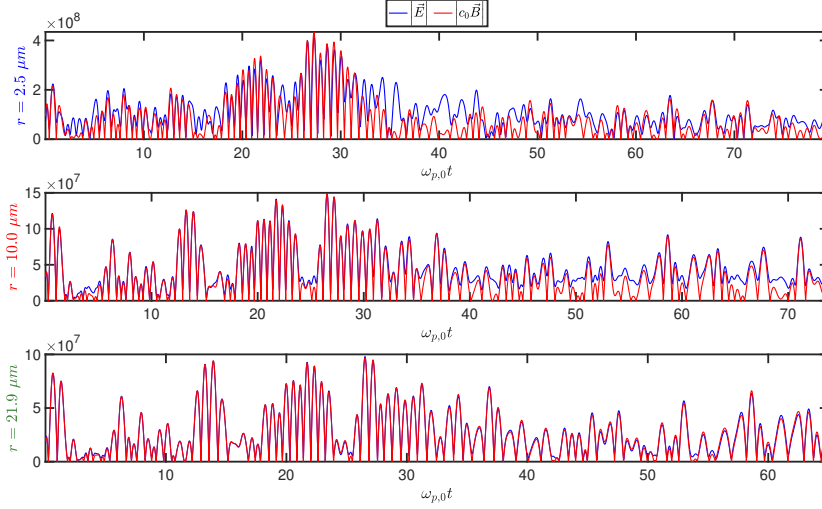


Figure 7: Comparison of  $|E_x|$  and  $|c_0 B_0|$  for the three probes. The large agreement at  $r = 10.0 \mu\text{m}$  suggests probes along this radius is near the far-field region, while the near-exact agreement at  $r = 21.9 \mu\text{m}$  suggests the probes along this radius lie in the far-field region.

#### 396 4.1. Collisionless Expansion Theory

397 There are several empirical equations to describe the total charge created by a hypere-  
398 locity impact of the form

$$399 \quad Q = Cm^a v^b, \quad (11)$$

400 where  $Q$  is the total charge created,  $m$  is the mass of the impactor in g,  $v$  is the speed of  
401 the impactor in km/s, and  $C$ ,  $a$ , and  $b$  are empirical coefficients. Typically,  $a$  is near unity,  
402 while  $b$  can range from 2.5 – 4.5 [21]. For our work, we use  $C = 6.13 \times 10^{-4}$ ,  $a = 1.02$ , and  
403  $b = 3.48$ . The penetration depth (and initial radius of the plasma) is given by the Frost  
404 equation:

$$405 \quad r_0 = km^{0.352} \delta^{0.167} v^{0.667}, \quad (12)$$

406 where  $r_0$  is penetration depth in cm,  $k$  is a constant dependent on the material,  $\delta$  is the  
407 density of the impactor in  $\text{g}/\text{cm}^3$ . We take the values of  $k = 0.42$  and  $\delta = 7.184 \text{ g}/\text{cm}^3$ ,  
408 the values for an aluminum target and iron impactor. Although a fully iron plasma in this  
409 work's simulations imply both target and impactor are composed of iron, the value of  $k$  for  
410 iron targets is not readily available, and thus aluminum is used as an approximation. The

411 following results still show reasonable agreement despite this. Assuming an initial spherical  
412 plasma, the initial (max) plasma density  $n_{e,0}$  is

$$413 \quad n_{e,0} = \frac{Q}{\frac{4}{3}\pi r_0^3 e}. \quad (13)$$

414 It is assumed that the plasma expands outward at the ion acoustic speed and that the ion  
415 acoustic speed is constant during expansion (*i.e.* the electron temperature is constant). The  
416 validity of this assumption is uncertain and will be assessed in a future work. If the plasma  
417 expands outward at the ion acoustic speed, then the plasma density as a function of time is

$$418 \quad n_e(t) = \frac{n_{e,0}}{\left(1 + \frac{c_s t}{r_0}\right)^3}, \quad (14)$$

419 where the ion acoustic speed  $c_s$  is

$$420 \quad c_s = \sqrt{\frac{\gamma k_B T_e}{m_i}}, \quad (15)$$

421  $k_B$  is the Boltzmann constant,  $T_e$  is the electron temperature, and  $m_i$  is the ion mass.

422 Assuming isothermal expansion,  $\gamma = 1$ .

423 From these assumptions, and following the work detailed by Close *et al.* [21], the electric  
424 field at the surface of the expanding plasma  $E_s(t)$  is

$$425 \quad E_s(t) = E_{s,0} \left(1 + \frac{c_s t}{r_0}\right)^{-9/4} \sin\left(\omega_{p,0} \frac{r_0}{c_s} \left[1 + \frac{c_s t}{r_0}\right]^{-1/2}\right), \quad (16)$$

426 where

$$427 \quad E_{s,0} = \sqrt{\frac{8k_B T_e n_{e,0}}{\pi \epsilon_0}}. \quad (17)$$

428 The electric field  $E_s(t)$  is composed of three different terms: an amplitude term  $E_{s,0}$  pro-  
429 portional to the square root of the electron temperature and density, a time decaying term  
430 resulting from the expansion of the plasma at the ion acoustic velocity, and a sinusoidal wave  
431 term. The term  $(1 + c_s t/r_0)^{-9/4}$  represents an attenuated amplitude weakening over time.

432 There are various differences between the assumptions behind this theory and the simu-  
433 lations presented here. The initial conditions of the PIC simulation are a simplified model  
434 based on the results of the hydrocodes developed by Fletcher *et al.* [15, 16] and assume an  
435 initial conical expansion of the plasma rather than a spherical expansion that the theory pre-  
436 scribes. In addition, the simulations have a nonuniform distribution in the plasma density

437 as opposed to the uniform distribution assumed here. For comparison, we will use the initial  
 438 max plasma density from the simulation for  $n_{e,0}$ . Despite this, the following subsection will  
 439 demonstrate that the theory and simulations show reasonable agreement.

#### 440 4.2. Validation with Theory

441 The Taylor expansion of  $(1 + c_s t/r_0)^{-1/2}$  centered about an arbitrary point  $t_0$  becomes

$$442 \left(1 + \frac{c_s t}{r_0}\right)^{-1/2} \approx \left(1 + \frac{c_s t_0}{r_0}\right)^{-1/2} - \frac{(t - t_0) c_s}{2 r_0} \left(1 + \frac{c_s t_0}{r_0}\right)^{-3/2}. \quad (18)$$

443 Applying this Taylor expansion into the sinusoidal term of Eq. (16) and assuming  $c_s t_0/r_0 \ll 1$   
 444 (*i.e.*, a short time after impact before expansion), the expression becomes

$$445 E_s(t) \approx -E_{s,0} \sin\left(\omega_{p,0} \frac{r_0}{c_s} - \frac{\omega_{p,0}}{2} t\right). \quad (19)$$

446 This is a valid assumption as, for our test case,  $c_s t_0/r_0 \approx 0.0025$  for a time corresponding  
 447 to 0.4 ps (the length of our simulation as a characteristic time length after impact). This  
 448 predicts that the electric field is a constant amplitude wave with amplitude  $E_{s,0}$  oscillating  
 449 at a frequency of  $\omega_{p,0}/2$ . This is similar to the simulation results. In Figure 4, the most  
 450 prominent signals correspond to frequencies in between  $\omega_{p,0}/2$  and  $\omega_{p,0}$ , showing agreement  
 451 in order of magnitude between the simulation and theory. Not represented in the theoretical  
 452 radiation are the multiple frequencies of the sinusoids prevalent in the simulation signals. An  
 453 explanation for this is the density gradient in the simulation plasma: with a density gradient,  
 454 the plasma frequency varies spatially while the theory is derived assuming a uniform density.  
 455 The existence of a density gradient means multiple plasma frequencies exist, allowing for  
 456 multiple frequencies to become prevalent. Nonetheless, both simulation and theory are  
 457 similar in magnitude, with further refinement of theory required in future works.

458 Figure 8 plots the amplitude of the electric field  $E_{s,0}$  over a range of impactor masses  
 459 and velocities. The electric field amplitude is on the order of  $10^8$  V/m, reaching  $10^9$  V/m  
 460 in the highest velocities and smallest masses. For a mass of 1 ng and a velocity of 20 km/s,  
 461 the theory predicts an electric field magnitude of  $2.7 \times 10^8$  V/m. This is comparable to the  
 462 electric field magnitude shown in Figure 1 showing good agreement in order of magnitude.  
 463 Furthermore, Figure 8 demonstrates that the highest risk threats related to the electric field

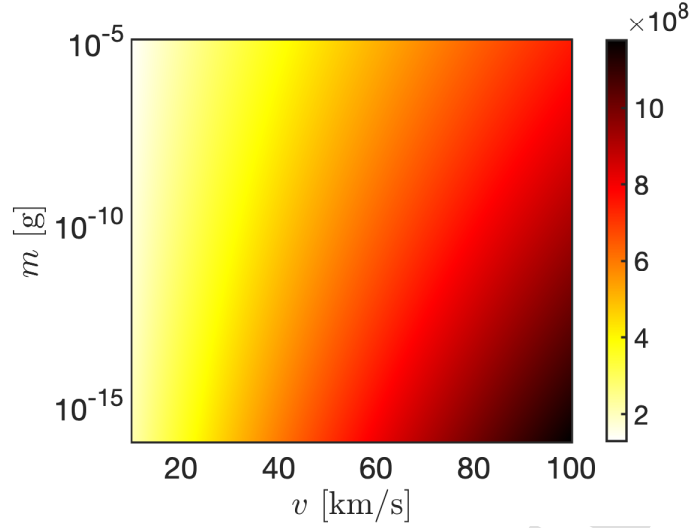


Figure 8: Amplitude  $E_{s,0}$  of the initial electric field  $E_s(t=0)$  at the surface of the expanding plasma in V/m at 2 eV.

464 originate from the smallest masses and highest velocities; this is due to the fact that the  
 465 degree of ionization scales with velocity, which corresponds to larger plasma densities and  
 466 electric fields. Since pressure is proportional to the square of the electric field, the highest  
 467 velocity particles can cause an increase in electric stress by two orders of magnitude relative  
 468 to the slower particles, providing an explanation of how this phenomenon can cause electrical  
 469 failure on spacecraft surface material.

470 Overall, the simulation shows agreement with both the theoretical amplitude and EMP  
 471 frequency. Both the theory and simulation provide an explanation for why spacecraft can  
 472 experience electrical damage; faster particles can increase the electric field experienced by one  
 473 order of magnitude, which increases the electric stress by two orders of magnitude. **Although**  
 474 **the electric field as the point of impact is very large, a 2D wave decays proportional to  $r^{-0.5}$**   
 475 **(and proportional to  $r^{-1}$  for a 3D wave). Thus, the electric field at a distance  $r$  away from**  
 476 **the impact point is**

$$477 \quad E(r) = E_{s,0} \left( \frac{L}{r} \right), \quad (20)$$

478 where  $L$  is some characteristic length of the plasma. Here, we use the decay of a 3D wave as  
 479 that is more realistic of what a spacecraft will experience. As an approximation of Eq. (20),

480 we let  $E_{s,0} \sim \mathcal{O}(10^8)$  V/m and  $L \sim \mathcal{O}(10^{-6})$  m, and

$$481 \quad E(r) \sim \mathcal{O}\left(\frac{100}{r}\right). \quad (21)$$

482 The given “rule of thumb” for spacecraft design is to use dielectric surfaces that are rated  
 483 to withstand electric fields less than  $2 \times 10^7$  V/m [32]. For  $E(r) < 2 \times 10^7$  V/m, this means  
 484 surfaces that are greater than  $5 \mu\text{m}$  away from an impact are sufficiently protected. This  
 485 is the vast majority of surfaces; however, during meteoroid showers, multiple impacts can  
 486 occur during a short time period. This higher meteoroid flux can cause prolonged stress over  
 487 a period of time rather than instantaneous stress. Moreover, the upper limit of  $2 \times 10^7$  V/m  
 488 may be lower due to geometries such as sharp corners and interfaces. Therefore, the electric  
 489 fields from hypervelocity impacts are generally sufficiently protected, but in edge cases may  
 490 cause significant damage.

#### 491 4.3. Comparison with Experimental Measurements

492 A direct, quantitative comparison between results reported in experiments and results  
 493 discussed from these simulations cannot be made because of discrepancies between experi-  
 494 mental and computational setups. For instance, the effects of various impactor and target  
 495 materials and the combinations of such are not included in current simulation capabili-  
 496 ties. Experiments conducted at the NASA AVGR facility maintained a vacuum pressure  
 497 of 0.5 Torr, where the background pressure introduced effects such as Rayleigh-Taylor and  
 498 Richtmyer-Meshov instabilities [19, 20]. Current simulation capabilities assume a true vac-  
 499 uum pressure with radiation in free space. The inclusion of a low-density background gas  
 500 species will be explored in a future work. Moreover, these simulations utilize the simplified  
 501 results of previous fluid simulations as the initial conditions, as discussed in Section 2.3. In  
 502 addition, the impactor masses and velocities differs from those explored in other experiments,  
 503 such as the work by Zhang *et al.* that analyzes microwave radiation from these impacts [10].  
 504 Despite these discrepancies, qualitative comparisons can be conducted.

505 Experiments were conducted in 2011 at the Max Planck Institute (MPI) for Nuclear  
 506 Physics [1, 33, 8]. This specific set of data is chosen to minimize deviations between experi-  
 507 ments and simulations; this specific set of data maintains lower vacuum pressure on the order  
 508 of  $\mu\text{Torr}$  and has impactor velocities and masses comparable to those simulated by Fletcher

509 *et al.* [15]. For the 315 MHz patch antennas in these experiments, signals for an impactor of  
 510 mass 1.4 fg at a velocity of 40 km/s were measured  $t_0 = 0.04 \mu\text{s}$  after impact approximately  
 511  $r = 30$  cm from the impact site. To be consistent with the results of the simulation, the  
 512 maximum plasma frequency should be on the RF band during this time. For a value of  
 513  $t_0 = 0.04 \mu\text{s}$ , the theoretical frequency of the radiation using Eq. (16) and Eq. (18) is 2452  
 514 MHz, which is within the ultra high frequency (UHF) radio band. Therefore, RF emissions  
 515 detected during this time frame are consistent with the simulation and theory. These simula-  
 516 tions are also consistent with the work reported by Zhang *et al.* in the microwaves measured  
 517 by hypervelocity impacts [10]. In their work, they correlate the experimental microwave  
 518 frequencies measured with the theoretical plasma frequency, showing they are on the same  
 519 order of magnitude, which is the same conclusion shown in Figure 4.

## 520 5. Conclusions and Future Work

521 Using a 2D DG-PIC model, we have shown that EMP can be spontaneously generated  
 522 after plasma production from hypervelocity impacts. This EMP shows nearly circular waves,  
 523 characterized by asymmetries and forking patterns, radiating from the point of the plasma  
 524 with the highest density. Furthermore, the EMP has characteristics similar to waves emitted  
 525 by antennas; waves closer to the plasma source will decay similarly to waves in the Fresnel  
 526 region of an antenna, while waves farther away decay similarly to far-field region waves,  
 527 decaying inversely proportional to the distance for a 3D wave and inversely proportional to  
 528 the square root of the distance for a 2D wave. The simulation also shows consistency with  
 529 what is predicted by theory and observed in experiments, with radiation frequency ranging  
 530 from  $\omega_{p,0}/2 - \omega_{p,0}$  and electric field magnitudes ranging from  $10^8 - 10^9$  V/m.

531 Our results have many academic and practical implications. Most notably, the radiation  
 532 of the plasma is limited by the plasma frequency associated with the point of largest density.  
 533 From an academic perspective, the emission mechanism associated with these frequencies is a  
 534 subject of interest. The cutoff frequency for an ordinary wave states that the lowest frequency  
 535 of emission possible is at minimum the plasma frequency. This shows the importance of  
 536 including the density gradient in the analysis of these plasmas, as the only explanation  
 537 for the radiation with frequency lower than the maximum plasma frequency is that there is

538 radiation associated with the edge plasma density, as discussed in Section 3. From a practical  
539 perspective, a measurement of the frequency of the EMP can estimate the maximum plasma  
540 density within an order of magnitude, and vice versa. Further work is required to validate  
541 this claim in the presence of other relevant physics previously discussed, such as charged  
542 target surfaces and dust.

543 Another important conclusion is that within a single impact, emission can span a wide  
544 range of frequencies, including both RF and microwave frequencies, resulting from the chang-  
545 ing plasma frequency as the plasma expands. In previous works, it has been hypothesized  
546 that emissions can span a wide range of frequencies as the velocity of the impactor is varied;  
547 however, this range of frequencies can still be seen in a single impact as opposed to several  
548 different impacts. If the emission is directly proportional to the plasma frequency, then the  
549 frequency of the radiation will be highest when the plasma density is highest (*i.e.*, right after  
550 impact) and decreases as the plasma density decreases. Near the initial impact, the plasma  
551 density will produce a plasma frequency that is at the visible light spectrum; therefore, the  
552 radiation will result in an optical flash of visible light [34, 35, 36]. As the plasma frequency  
553 decreases into the microwave and radio frequency spectra, EMPs of those frequencies can  
554 be measured [1, 10]. Thus, the mechanisms behind these different phenomena may be the  
555 same mechanism, suggesting they are actually the same phenomenon. In reality, it is likely  
556 that many different mechanisms exist in producing these different phenomena, and the ex-  
557 act mechanism behind the emission in this work may or may not be the most influential.  
558 Nonetheless, there is a proportionality between plasma frequency (and the square root of the  
559 plasma density) and the EMP frequency. Therefore, understanding the plasma expansion  
560 process and the radiation mechanism is important in understanding which frequencies are  
561 most prevalent throughout the impact duration.

562 Future work will focus on improving the limitations of computational and theoretical  
563 models by addressing missing physics. For instance, experiments were conducted on biased  
564 targets charged to up to 1000 V, while current simulation and theory do not model reflections  
565 from the impact surface nor surface charging effects. With a charged surface, a background  
566 electric field will exist, which will disperse and expand the plasma more quickly than without  
567 a field. As a result, the temporal decay of the EMP will be quicker, leading the EMP

568 to reach a smaller frequency in a shorter amount of time. Longer simulations spanning  
 569 microseconds are also an unexplored area, which allows for a direct comparison between  
 570 simulation and experiments. In particular, the validation of the temporal decay term in  
 571 Eq. (16),  $(1 + c_s t / r_0)^{-9/4}$ , is currently not possible because of the short simulation length  
 572 resulting from the strict time step requirements of the DG-PIC model. Finally, the theory  
 573 used to derive Eq. (16) and Eq. (18) uses a uniform plasma and includes only electrostatic  
 574 effects, neglecting higher order effects such as self-induced magnetic fields. The theory  
 575 proposed by Close *et al.* [21] can be reformulated using an electromagnetic approach to  
 576 address radiation and other electromagnetic phenomenon.

### 577 Acknowledgements

578 This material is based upon work supported by the National Science Foundation Graduate  
 579 Research Fellowship under Grant No. 1656518 and the Department of Energy grant DE-  
 580 SC0024584. This work used the Extreme Science and Engineering Discovery Environment  
 581 (XSEDE), which is supported by National Science Foundation grant number ACI-1548562.

### 582 Appendix A. Derivation of PHM-PML Equations

583 A set of hyperbolic PDEs in conservation form is written as

$$584 \frac{\partial \mathbf{u}}{\partial t} + \nabla \cdot \mathbf{F} = \mathbf{S}, \quad (A.1)$$

586 where  $\mathbf{u}$  is the state vector,  $\mathbf{F} = \mathbf{F}(\mathbf{u})$  is the flux matrix, and  $\mathbf{S}$  is the source vector. In 2D  
 587 Cartesian coordinates, Eq. (A.1) is written as:

$$588 \frac{\partial \mathbf{u}}{\partial t} + \frac{\partial \mathbf{F}_x}{\partial x} + \frac{\partial \mathbf{F}_y}{\partial y} = \mathbf{S}, \quad (A.2)$$

590 where  $\mathbf{F}_j = \mathbf{F}_j(\mathbf{u})$  is the flux vector in the  $j$  direction for  $j = x, y$ . For the case of  
 591 the PHM equations, Eq. (4),  $\mathbf{u} = [E_x \ E_y \ B_z \ \phi]^T$ ,  $\mathbf{F}_x = [\chi\phi \ B_z \ E_y \ \chi E_x]^T$ ,  $\mathbf{F}_y =$   
 592  $[-B_z \ \chi\phi \ -E_x \ \chi E_y]^T$ , and  $\mathbf{S} = [-j_x \ -j_y \ 0 \ \chi\rho]^T$ ,

593 The complex-coordinate transformation for PMLs assumes that the state vector  $\mathbf{u}$  takes  
 594 on a wave form  $\mathbf{u} = \mathbf{u}_0 \exp(i(\mathbf{k} \cdot \mathbf{x} - \omega t))$ , where  $\mathbf{u}_0$  is some waveform amplitude,  $\mathbf{k}$  is the  
 595 wavevector, and  $\omega$  is the wave frequency. Then, a coordinate transformation is introduced to

596 transform Eq. (A.2) from the purely real axis onto the complex plane. This transformation  
597 is given as

$$598 \quad \frac{\partial}{\partial x} \rightarrow \frac{1}{1 + \frac{i\sigma_x}{\omega}} \frac{\partial}{\partial x} = \left(1 - \frac{\sigma_x}{\sigma_x - i\omega}\right) \frac{\partial}{\partial x}, \quad (A.3)$$

600 where  $\sigma_x = \sigma_x(x)$  is the artificial damping coefficient in the  $x$  direction [37]. The form of  
601  $\sigma_x(x)$  is chosen by the user, but typically starts at zero and grows towards the maximum  
602 damping value from the inner edge to the outer edge of the PML. A similar transformation  
603 is done in the  $y$  direction. Substituting the transformation for the  $x$  and  $y$  directions and  
604 replacing  $\frac{\partial}{\partial t}$  with  $-i\omega$ , Eq. (A.2) becomes

$$605 \quad -i\omega \mathbf{u} + \frac{\partial \mathbf{F}_x}{\partial x} + \frac{\partial \mathbf{F}_y}{\partial y} = \mathbf{S} + \left(\frac{\sigma_x}{\sigma_x - i\omega}\right) \frac{\partial \mathbf{F}_x}{\partial x} + \left(\frac{\sigma_y}{\sigma_y - i\omega}\right) \frac{\partial \mathbf{F}_y}{\partial y}. \quad (A.4)$$

607 From here we define auxiliary variables  $\mathbf{P}_x$  and  $\mathbf{P}_y$  as

$$608 \quad \mathbf{P}_x = \frac{-1}{\sigma_x - i\omega} \frac{\partial \mathbf{F}_x}{\partial x}, \quad (A.5)$$

$$609 \quad \mathbf{P}_y = \frac{-1}{\sigma_y - i\omega} \frac{\partial \mathbf{F}_y}{\partial y}. \quad (A.6)$$

611 With some rearrangement, the auxiliary variables can be written as

$$612 \quad -i\omega \mathbf{P}_x + \frac{\partial \mathbf{F}_x}{\partial x} = -\sigma_x \mathbf{P}_x, \quad (A.7)$$

$$613 \quad -i\omega \mathbf{P}_y + \frac{\partial \mathbf{F}_y}{\partial y} = -\sigma_y \mathbf{P}_y. \quad (A.8)$$

615 Substituting Eqs. (A.5) and (A.6) into Eq. (A.4) and replacing all  $-i\omega$  terms with  $\frac{\partial}{\partial t}$  in Eqs.  
616 (A.4), (A.7), and (A.8) results in a new system of PDEs:

$$617 \quad \frac{\partial \mathbf{u}}{\partial t} + \frac{\partial \mathbf{F}_x}{\partial x} + \frac{\partial \mathbf{F}_y}{\partial y} = \mathbf{S} - \sigma_x \mathbf{P}_x - \sigma_y \mathbf{P}_y, \quad (A.9)$$

$$618 \quad \frac{\partial \mathbf{P}_x}{\partial t} + \frac{\partial \mathbf{F}_x}{\partial x} = -\sigma_x \mathbf{P}_x, \quad (A.10)$$

$$619 \quad \frac{\partial \mathbf{P}_y}{\partial t} + \frac{\partial \mathbf{F}_y}{\partial y} = -\sigma_y \mathbf{P}_y. \quad (A.11)$$

621 The final set of equations to be solved is presented as

$$622 \quad \frac{\partial \mathbf{u}'}{\partial t} + \frac{\partial \mathbf{F}'_x}{\partial x} + \frac{\partial \mathbf{F}'_y}{\partial y} = \mathbf{S}', \quad (A.12)$$

624 where

$$625 \quad \mathbf{u}' = \begin{bmatrix} \mathbf{u} \\ \mathbf{P}_x \\ \mathbf{P}_y \end{bmatrix}, \quad (\text{A.13})$$

$$626 \quad \mathbf{F}'_x = \begin{bmatrix} \mathbf{F}_x(\mathbf{u}) \\ \mathbf{F}_x(\mathbf{u}) \\ \mathbf{0} \end{bmatrix}, \quad (\text{A.14})$$

$$627 \quad \mathbf{F}'_y = \begin{bmatrix} \mathbf{F}_y(\mathbf{u}) \\ \mathbf{0} \\ \mathbf{F}_y(\mathbf{u}) \end{bmatrix}, \quad (\text{A.15})$$

$$628 \quad \mathbf{S}' = \begin{bmatrix} \mathbf{S} - \sigma_x \mathbf{P}_x - \sigma_y \mathbf{P}_y \\ -\sigma_x \mathbf{P}_x \\ -\sigma_y \mathbf{P}_y \end{bmatrix}. \quad (\text{A.16})$$

629  
630 To prevent mitigate numerical error associated with the divergence correction of the PHM  
631 equations, we include the damping coefficients discussed by Copplestone *et al.* [26], given as

$$632 \quad \phi(1 - \epsilon) \rightarrow \phi, \quad (\text{A.17})$$

633 where  $\epsilon$  is a small numerical parameter and is conducted before every level of the Runge-  
634 Kutta update. This prevents the numerical error associated with the auxiliary PML values  
635 from becoming too large.

## 636 Appendix B. Derivation of PML Numerical Fluxes

637 This section is separated into two subsections: first, a derivation of numerical fluxes for  
638 the original PHM equations, following a derivation of numerical fluxes for the augmented  
639 PHM equations including PMLs (*i.e.* the PHM-PML equations).

640 *Appendix B.1. Numerical Fluxes without PML*

641 For an equation in 2D conservation form, as defined by Eq. (A.2), the corresponding 1D  
642 initial value Riemann problem (RP) is written as

$$643 \quad \frac{\partial \mathbf{u}}{\partial \tau} + \mathbb{A} \frac{\partial \mathbf{u}}{\partial \zeta} = \mathbf{0}; \quad (\text{B.1})$$

$$644 \quad \mathbf{u}(\zeta, 0) = \begin{cases} \mathbf{u}_L & \text{if } \zeta < 0 \\ \mathbf{u}_R & \text{if } \zeta > 0 \end{cases}, \quad (\text{B.2})$$

645 where  $\tau$  and  $\zeta$  are dummy variables for time and the spatial direction normal to the element  
646 edge,  $\mathbb{A} = n_x \frac{\partial \mathbf{F}_x}{\partial \mathbf{u}} + n_y \frac{\partial \mathbf{F}_y}{\partial \mathbf{u}}$  is the characteristic matrix composed of the Jacobians of the flux  
647 vector dotted in the normal direction  $\hat{n} = [n_x \ n_y]^T$ , and  $\mathbf{u}_L$  and  $\mathbf{u}_R$  are the state vectors  
648 for the left and right side. Here, we use the nomenclature that the left ( $L$ ) refers to the  
649 inside of the element and the right ( $R$ ) symbol corresponds to the outside of the element.  
650 Assuming that  $\mathbb{A}$  is diagonalizable (i.e., all eigenvalues are real with a unique and complete  
651 set of eigenvectors),  $\mathbb{A}$  can be written as

$$653 \quad \mathbb{A} = R \Lambda R^{-1}, \quad (\text{B.3})$$

654 where  $\Lambda$  is a diagonal matrix consisting of the eigenvalues of  $\mathbb{A}$ , the columns of  $R$  are the  
655 corresponding right eigenvectors, and the rows of  $R^{-1}$  are the corresponding left eigenvectors.  
656 For the PHM equations,  $R$  and  $\Lambda$  are constant valued, meaning the PHM equations are linear.  
657 The eigenvalues represent the propagation velocities (characteristics) of certain characteristic  
658 variables  $\mathbf{v}$  of the wave, which can be found as

$$660 \quad \mathbf{v} = R^{-1} \mathbf{u}. \quad (\text{B.4})$$

661 Let  $n$  represent the number of states of vector  $\mathbf{u}$ . By recasting Eq. (B.1) into characteristic  
662 variables, this creates a set of  $n$  uncoupled PDEs given by

$$664 \quad \frac{\partial \mathbf{v}}{\partial \tau} + \Lambda \frac{\partial \mathbf{v}}{\partial \zeta} = \mathbf{0}; \quad (\text{B.5})$$

$$665 \quad \mathbf{v}(\zeta, 0) = \begin{cases} \mathbf{v}_L & \text{if } \zeta < 0 \\ \mathbf{v}_R & \text{if } \zeta > 0 \end{cases}, \quad (\text{B.6})$$

667 where  $\mathbf{v}_L$  and  $\mathbf{v}_R$  are the characteristic variable vectors for the left and right side.

668 For  $i = 1, \dots, n$ , the solution of the  $i^{\text{th}}$  PDE of Eq. (B.5) is

$$669 \quad v_i(\zeta, \tau) = v_i(\zeta - \lambda_i \tau, 0), \quad (B.7)$$

671 where  $\lambda_i$  is the  $i^{\text{th}}$  eigenvalue given by  $\Lambda$ . The characteristic variables at the cell interface  
672  $\zeta = 0$  are then

$$673 \quad v_i(0, \tau) = v_i(-\lambda_i \tau, 0) = v_i^*, \quad (B.8)$$

675 where the star symbol (\*) is used to denote a variable at the cell interface. Thus, each  
676 characteristic variable at the cell interface can be explicitly expressed as

$$677 \quad v_i^* = \begin{cases} v_{L,i} & \text{if } \lambda_i > 0 \\ v_{R,i} & \text{if } \lambda_i < 0 \\ \frac{v_{L,i} + v_{R,i}}{2} & \text{if } \lambda_i = 0 \end{cases} \quad (B.9)$$

678  
679 Since the PHM equations are linear, the state vector at the cell interface (or interfacial state  
680 vector) is connected through the integral curve,

$$681 \quad \tilde{\mathbf{u}}^* = R\mathbf{v}^*. \quad (B.10)$$

683 Here, we denote the use of a tilde for clarification between two similar yet slightly different  
684 variables in the following subsection. The corresponding flux matrix is

$$685 \quad \mathbf{F}^* = \mathbf{F}(\tilde{\mathbf{u}}^*). \quad (B.11)$$

## 687 *Appendix B.2. Numerical Fluxes with PML*

688 The corresponding RP for the 2D augmented PML-PHM system, Eq. (A.12), is

$$689 \quad \frac{\partial \mathbf{u}'}{\partial \tau} + \mathbb{A}' \frac{\partial \mathbf{u}'}{\partial \zeta} = \mathbf{0}; \quad (B.12)$$

$$690 \quad \mathbf{u}'(\zeta, 0) = \begin{cases} \mathbf{u}'_L & \text{if } \zeta < 0 \\ \mathbf{u}'_R & \text{if } \zeta > 0 \end{cases}, \quad (B.13)$$

692 where prime (') values correspond to values in the new augmented PML system of equations.

693 Here,  $\mathbf{u}'$  (given by Eq. (A.13)) is the modified state vector to include the auxiliary variables

694 related to the PML layers that are coupled to the fluxes. From Eq. (A.13), the new system  
 695 is at most  $3n$  elements long. The end goal is to derive an expression for the interfacial  
 696 state values  $(\mathbf{u}')^* = [\mathbf{u}^* \ \mathbf{P}_x^* \ \mathbf{P}_y^*]^T$  which can then be used to derive a numerical flux. As  
 697 a reminder,  $\tilde{\mathbf{u}}^*$  is the interfacial state vector for the original system of equations without  
 698 PML implementation in Eq. (B.10). The tilde is used to highlight the fact that this original  
 699 interfacial state vector  $\tilde{\mathbf{u}}^*$  cannot be said to be the same as  $\mathbf{u}^*$  defined within  $(\mathbf{u}')^*$  without  
 700 proof.

701 Let  $\mathbf{0}_{a \times b}$  denote an  $a \times b$  zero matrix. Then,

$$702 \quad \mathbb{A}' = n_x \frac{\partial \mathbf{F}'_x}{\partial \mathbf{u}'} + n_y \frac{\partial \mathbf{F}'_y}{\partial \mathbf{u}'} = \begin{bmatrix} \mathbb{A} & \mathbf{0}_{n \times n} & \mathbf{0}_{n \times n} \\ n_x \frac{\partial \mathbf{F}'_x}{\partial \mathbf{u}} & \mathbf{0}_{n \times n} & \mathbf{0}_{n \times n} \\ n_y \frac{\partial \mathbf{F}'_y}{\partial \mathbf{u}} & \mathbf{0}_{n \times n} & \mathbf{0}_{n \times n} \end{bmatrix}. \quad (\text{B.14})$$

703  
 704 From inspection, the eigenvalues of  $\mathbb{A}'$  are the eigenvalues of  $\mathbb{A}$  with additional eigenvalues  
 705 of 0 with multiplicity  $2n$ . In other words,

$$706 \quad \Lambda' = \begin{bmatrix} \Lambda & \mathbf{0}_{n \times 2n} \\ \mathbf{0}_{2n \times n} & \mathbf{0}_{2n \times 2n} \end{bmatrix}. \quad (\text{B.15})$$

707  
 708 The right eigenvalues of  $\Lambda'$  can be found via solving

$$709 \quad \Lambda' R' = R' \Lambda'. \quad (\text{B.16})$$

710  
 711  $R'$  takes the form

$$712 \quad R' = \begin{bmatrix} R & \mathbf{0}_{n \times 2n} \\ C & D \end{bmatrix}, \quad (\text{B.17})$$

713  
 714 where  $C = \begin{bmatrix} R_{21} \\ R_{31} \end{bmatrix}$ ,  $D = \begin{bmatrix} R_{22} & R_{23} \\ R_{32} & R_{33} \end{bmatrix}$ , and  $R$  is the right eigenvector matrix of the original  
 715 system  $\mathbb{A}R = R\Lambda$  (cf. Eq. (B.3)). The explicit expressions for  $C$  and  $D$  will not matter in  
 716 the end result.

717 We assume that  $C$  and  $D$  can be derived such that  $R'$  contains a unique set of eigenvectors  
 718 and that  $D$  is invertible. For the case in which the eigenvalues of the original system,  $\Lambda$ , are  
 719 all non-zero, this can be easily proven. Since all eigenvalues of  $\Lambda'$  are real and  $R'$  contains a

720 unique set of eigenvectors,  $\mathbb{A}'$  is diagonalizable and  $(R')^{-1}$  exists. To find the left eigenvectors  
 721  $(R')^{-1}$ , one can use the formula for inverting  $2 \times 2$  block matrices [38]. This comes out to

$$722 \quad (R')^{-1} = \begin{bmatrix} R^{-1} & \mathbf{0}_{n \times 2n} \\ -D^{-1}CR^{-1} & D^{-1} \end{bmatrix}. \quad (\text{B.18})$$

723  
 724 Following the same procedure as the original system, and taking advantage of the linear  
 725 nature of the PHM-PML equations, the characteristic variable vector is

$$726 \quad \mathbf{v}' = \begin{bmatrix} R^{-1}\mathbf{u} \\ -D^{-1}CR^{-1}\mathbf{u} + D^{-1}\mathbf{P} \end{bmatrix}. \quad (\text{B.19})$$

727  
 728 where  $\mathbf{P} = \begin{bmatrix} \mathbf{P}_x & \mathbf{P}_y \end{bmatrix}^T$ . Thus, the first  $n$  characteristic variables of  $\mathbf{v}'$  are  $\mathbf{v}$ . The interfacial  
 729 state values are then given by

$$730 \quad (\mathbf{u}')^* = \begin{bmatrix} \mathbf{u}^* \\ \mathbf{P}_x^* \\ \mathbf{P}_y^* \end{bmatrix} = (R')(\mathbf{v}')^*. \quad (\text{B.20})$$

731  
 732 The fluxes for the PML system are not functions of the auxiliary variables as shown by  
 733 Eq. (B.11). As a result, it does not matter what  $\mathbf{P}_x^*$  and  $\mathbf{P}_y^*$  are for the purpose of deriving  
 734 a numerical flux; therefore, we only need to derive an expression for  $\mathbf{u}^*$ . From Eq. (B.20),

$$735 \quad (\mathbf{u}')^* = R(\mathbf{v}')^*(\mathbf{v}')^*. \quad (\text{B.21})$$

736  
 737 However, this is the exact same expression for the interfacial states without the PML media,  
 738 Eq. (B.10). The expression for the interfacial states of the non-auxiliary variables are the  
 739 same regardless of whether PML media are implemented or not, or simply stated,

$$740 \quad \mathbf{u}^* = \tilde{\mathbf{u}}^*. \quad (\text{B.22})$$

741  
 742 This significantly simplifies the derivation of the numerical flux. As discussed previously  
 743 the modified flux vectors of the PML system  $\mathbf{F}'_x = \mathbf{F}'_x(\mathbf{u})$  and  $\mathbf{F}'_y = \mathbf{F}'_y(\mathbf{u})$  are given by Eqs.  
 744 (A.14) and (A.15). Therefore, the interfacial fluxes  $(\mathbf{F}'_x)^*$  and  $(\mathbf{F}'_y)^*$  are given as

$$745 \quad (\mathbf{F}'_x)^* = \begin{bmatrix} \mathbf{F}_x(\tilde{\mathbf{u}}^*) \\ \mathbf{F}_x(\tilde{\mathbf{u}}^*) \\ \mathbf{0} \end{bmatrix}, (\mathbf{F}'_y)^* = \begin{bmatrix} \mathbf{F}_y(\tilde{\mathbf{u}}^*) \\ \mathbf{0} \\ \mathbf{F}_y(\tilde{\mathbf{u}}^*) \end{bmatrix}, \quad (\text{B.23})$$

747 Therefore, the 2D flux normal to the cell interface (or interfacial flux) is

$$748 \quad (\mathbf{F}'_n)^* = \hat{\mathbf{n}} \cdot (\mathbf{F}')^* = \begin{bmatrix} n_x \mathbf{F}_x(\tilde{\mathbf{u}}^*) + n_y \mathbf{F}_y(\tilde{\mathbf{u}}^*) \\ n_x \mathbf{F}_x(\tilde{\mathbf{u}}^*) \\ n_y \mathbf{F}_y(\tilde{\mathbf{u}}^*) \end{bmatrix}. \quad (\text{B.24})$$

749

## 750 References

- 751 [1] S. Close, I. Linscott, N. Lee, T. Johnson, D. Strauss, A. Goel, A. Fletcher, D. Lauben,  
752 R. Srama, A. Mocker, S. Bugiel, Detection of electromagnetic pulses produced by hy-  
753 pervelocity micro particle impact plasmas, *Physics of Plasmas* 20 (9) (2013) 092102.  
754 doi:10.1063/1.4819777.  
755 URL <https://aip.scitation.org/doi/abs/10.1063/1.4819777>
- 756 [2] J. McDonnell, N. McBride, D. Gardner, The Leonid Meteoroid Stream: Spacecraft  
757 Interactions and Effects, *Proceedings of the Second European Conference on Space*  
758 *Debris* (1997) 391.
- 759 [3] A. Goel, S. Close, Electrical anomalies on spacecraft due to hypervelocity impacts, in:  
760 2015 IEEE Aerospace Conference, 2015.
- 761 [4] R. D. Caswell, N. McBride, A. Taylor, Olympus end of life anomaly - a perseid mete-  
762 roid impact event?, *International Journal of Impact Engineering* 17 (1995) 139–150.  
763 doi:10.1016/0734-743X(95)99843-G.
- 764 [5] S. Close, S. M. Hunt, M. J. Minardi, F. M. McKeen, Analysis of perseid meteor head  
765 echo data collected using the advanced research projects Agency Long-Range Track-  
766 ing and Instrumentation Radar (ALTAIR), *Radio Science* 35 (5) (2000) 1233–1240.  
767 doi:10.1029/1999RS002277.
- 768 [6] M. C. Kelley, S. Pancoast, S. Close, Z. Wang, Analysis of electromagnetic and elec-  
769 trostatic effects of particle impacts on spacecraft, *Advances in Space Research* 49 (6)  
770 (2012) 1029–1033. doi:10.1016/j.asr.2011.12.023.

- 771 [7] R. Bianchi, F. Capaccioni, P. Cerroni, M. Coradini, E. Flamini, P. Hurren, G. Martelli,  
772 P. Smith, Radiofrequency emissions observed during macroscopic hypervelocity impact  
773 experiments, *Nature* 304 (26) (1984) 830–832. doi:10.1038/308830a0.
- 774 [8] N. Lee, S. Close, A. Goel, D. Lauben, I. Linscott, T. Johnson, D. Strauss, S. Bugiel,  
775 A. Mocker, R. Srama, Theory and experiments characterizing hypervelocity impact  
776 plasmas on biased spacecraft materials, *Physics of Plasmas* 20 (3) (2013) 032901.  
777 doi:10.1063/1.4794331.  
778 URL <https://aip.scitation.org/doi/abs/10.1063/1.4794331>
- 779 [9] K. Maki, E. Soma, T. Takano, A. Fujiwara, A. Yamori, Dependence of microwave  
780 emissions from hypervelocity impacts on the target material, *Journal of Applied Physics*  
781 97 (10) (2005) 104911. doi:10.1063/1.1896092.
- 782 [10] K. Zhang, Q. Zhang, R. Long, W. Liu, Time-frequency characteristics of microwaves  
783 generated by hypervelocity impact, *International Journal of Impact Engineering* 174  
784 (2023) 104505. doi:10.1016/J.IJIMPENG.2023.104505.
- 785 [11] D. M. Malaspina, G. Stenborg, D. Mehoke, A. Al-Ghazwi, M. M. Shen, H.-W.  
786 Hsu, K. Iyer, S. D. Bale, T. D. d. Wit, Clouds of Spacecraft Debris Liberated by  
787 Hypervelocity Dust Impacts on Parker Solar Probe, *The Astrophysical Journal* 925 (1)  
788 (2022) 27. doi:10.3847/1538-4357/AC3BBB.  
789 URL <https://iopscience.iop.org/article/10.3847/1538-4357/ac3bbb>  
790 <https://iopscience.iop.org/article/10.3847/1538-4357/ac3bbb/meta>
- 791 [12] H. B. Garrett, S. Close, Impact-induced ESD and EMI/EMP effects on space-  
792 craft - A review, *IEEE Transactions on Plasma Science* 41 (12) (2013) 3545–3557.  
793 doi:10.1109/TPS.2013.2286181.
- 794 [13] S. T. Islam, W. Ma, J. G. Michopoulos, K. Wang, Plasma formation in ambi-  
795 ent fluid from hypervelocity impacts, *Extreme Mechanics Letters* 58 (2022) 101927.  
796 doi:10.1016/j.eml.2022.101927.

- 797 [14] S. T. Islam, W. Ma, J. G. Michopoulos, K. Wang, Plasma formation in am-  
798 biant fluid from hypervelocity impacts, *Extreme Mechanics Letters* 58 (1 2023).  
799 doi:10.1016/j.eml.2022.101927.
- 800 [15] A. C. Fletcher, S. Close, D. Mathias, Simulating plasma production from hypervelocity  
801 impacts, *Physics of Plasmas* 22 (9) (2015) 093504. doi:10.1063/1.4930281.  
802 URL <https://aip.scitation.org/doi/abs/10.1063/1.4930281>
- 803 [16] A. C. Fletcher, S. Close, Particle-in-cell simulations of an RF emission mechanism as-  
804 sociated with hypervelocity impact plasmas, *Physics of Plasmas* 24 (5) (2017) 053102.  
805 doi:10.1063/1.4980833.  
806 URL <https://aip.scitation.org/doi/abs/10.1063/1.4980833>
- 807 [17] R. V. Kennedy, J. E. Allen, The floating potential of spherical probes and dust  
808 grains. II: Orbital motion theory, *Journal of Plasma Physics* 69 (6) (2003) 485–506.  
809 doi:10.1017/S0022377803002265.  
810 URL <https://www.cambridge.org/core/journals/journal-of-plasma-physics/article/floati>
- 811 [18] G. Shohet, B. Estacio, I. Matthews, S. A. Young, N. Lee, S. Close, Micro-  
812 scopic ejecta measurements from hypervelocity impacts on aluminum and powdered  
813 regolith targets, *International Journal of Impact Engineering* 152 (2021) 103840.  
814 doi:10.1016/j.ijimpeng.2021.103840.
- 815 [19] B. Estacio, G. Shohet, S. A. Young, I. Matthews, N. Lee, S. Close, Dust and atmo-  
816 spheric influence on plasma properties observed in light gas gun hypervelocity im-  
817 pact experiments, *International Journal of Impact Engineering* 151 (2021) 103833.  
818 doi:10.1016/j.ijimpeng.2021.103833.  
819 URL [doi.org/10.1016/j.ijimpeng.2021.103833](https://doi.org/10.1016/j.ijimpeng.2021.103833)
- 820 [20] B. Estacio, S. A. Young, N. Lee, S. Elschot, Experimental evidence of rapid target charg-  
821 ing electromagnetic pulse from hypervelocity impact, *International Journal of Impact*  
822 *Engineering* 173 (3 2023). doi:10.1016/j.ijimpeng.2022.104473.

- 823 [21] S. Close, P. Colestock, L. Cox, M. Kelley, N. Lee, Electromagnetic pulses generated  
824 by meteoroid impacts on spacecraft, *Journal of Geophysical Research: Space Physics*  
825 115 (12) (2010) 12328. doi:10.1029/2010JA015921.  
826 URL <https://agupubs.onlinelibrary.wiley.com/doi/full/10.1029/2010JA015921>  
827 <https://agupubs.onlinelibrary.wiley.com/doi/abs/10.1029/2010JA015921>  
828 <https://agupubs.onlinelibrary.wiley.com/doi/10.1029/2010JA015921>
- 829 [22] G. B. Jacobs, J. S. Hesthaven, High-order nodal discontinuous Galerkin particle-in-cell  
830 method on unstructured grids, *Journal of Computational Physics* 214 (1) (2006) 96–121.  
831 doi:10.1016/j.jcp.2005.09.008.
- 832 [23] J. R. Angus, A. Link, A. Friedman, D. Ghosh, J. D. Johnson, On numerical energy con-  
833 servation for an implicit particle-in-cell method coupled with a binary Monte-Carlo  
834 algorithm for Coulomb collisions, *Journal of Computational Physics* 456 (5 2022).  
835 doi:10.1016/j.jcp.2022.111030.
- 836 [24] R. Lau, N. Lee, S. Elschot, Collisional particle-in-cell investigations of electromagnetic  
837 pulses in hypervelocity impact plasmas, *International Journal of Impact Engineering*  
838 (2023) 104692doi:10.1016/J.IJIMPENG.2023.104692.  
839 URL <https://linkinghub.elsevier.com/retrieve/pii/S0734743X23002038>
- 840 [25] J. S. Hesthaven, T. Warburton, *Nodal Discontinuous Galerkin Methods: Algorithms,*  
841 *Analysis, and Applications*, Springer, New York, 2007.
- 842 [26] S. M. Copplestone, P. Ortwein, C. D. Munz, Complex-Frequency Shifted PMLs for  
843 Maxwell’s Equations with Hyperbolic Divergence Cleaning and Their Application in  
844 Particle-in-Cell Codes, *IEEE Transactions on Plasma Science* 45 (1) (2017) 2–14.  
845 doi:10.1109/TPS.2016.2637061.
- 846 [27] P. O. Persson, G. Strang, A simple mesh generator in MATLAB, *SIAM Review* 46 (2)  
847 (2004) 329–345. doi:10.1137/S0036144503429121.
- 848 [28] D. A. Tidman, Radio Emission by Plasma Oscillations in Nonuniform Plasmas\*, *Phys-*  
849 *ical Review* 117 (2) (1960).

- 850 [29] D. A. Tidman, J. M. Boyd, Radiation by plasma oscillations incident on a density  
851 discontinuity, *Physics of Fluids* 5 (2) (1962) 213–218. doi:10.1063/1.1706598.
- 852 [30] J. P. Rayner, A. P. Whichello, D. Cheetham, Physical characteristics of plasma  
853 antennas, *IEEE Transactions on Plasma Science* 32 (1 III) (2004) 269–281.  
854 doi:10.1109/TPS.2004.826019.
- 855 [31] H. Q. Ye, M. Gao, C. J. Tang, Radiation theory of the plasma antenna,  
856 *IEEE Transactions on Antennas and Propagation* 59 (5) (2011) 1497–1502.  
857 doi:10.1109/TAP.2011.2123051.
- 858 [32] H. B. Garrett, A. C. Whittlesey, *Guide to Mitigating Spacecraft Charging Effects*, Vol. 3,  
859 2012.
- 860 [33] N. Lee, S. Close, D. Lauben, I. Linscott, A. Goel, T. Johnson, J. Yee, A. C. Fletcher,  
861 R. Srama, S. Bugiel, A. Mocker, P. Colestock, S. Green, Measurements of freely-  
862 expanding plasma from hypervelocity impacts, *International Journal of Impact En-  
863 gineering* 44 (2012) 40–49. doi:10.1016/j.ijimpeng.2012.01.002.
- 864 [34] A. Goel, N. Lee, S. Close, Estimation of hypervelocity impact parameters from mea-  
865 surements of optical flash, *International Journal of Impact Engineering* 84 (2015) 54–63.  
866 doi:10.1016/j.ijimpeng.2015.05.008.
- 867 [35] Y. M. Hew, A. Goel, S. Close, N. Lee, Hypervelocity impact flash and plasma on  
868 electrically biased spacecraft surfaces, *International Journal of Impact Engineering* 121  
869 (2018) 1–11. doi:10.1016/j.ijimpeng.2018.05.008.
- 870 [36] Y. M. Hew, S. Close, Hypervelocity impact flash expansion geometry under various  
871 spacecraft surface electrical conditions, *International Journal of Impact Engineering*  
872 150 (2021) 103792. doi:10.1016/j.ijimpeng.2020.103792.
- 873 [37] S. G. Johnson, *Notes on Perfectly Matched Layers (PMLs)* (2021).  
874 URL <http://arxiv.org/abs/2108.05348>
- 875 [38] T. T. Lu, S. H. Shiou, Inverses of  $2 \times 2$  block matrices, *Computers and Mathematics*  
876 *with Applications* 43 (1-2) (2002) 119–129. doi:10.1016/S0898-1221(01)00278-4.

**Raymond Lau** - Conceptualization, Methodology, Software, Validation, Formal Analysis, Investigation, Writing - Original Draft, Writing - Review & Editing, Visualization

**Nicolas Lee** - Conceptualization, Resources, Writing - Original Draft, Supervision, Project Administration, Funding Acquisition

**Sigrid Elschot** - Conceptualization, Resources, Writing - Original Draft, Supervision, Project Administration, Funding Acquisition

**Declaration of interests**

The authors declare that they have no known competing financial interests or personal relationships that could have appeared to influence the work reported in this paper.

The authors declare the following financial interests/personal relationships which may be considered as potential competing interests:

Raymond Lau reports financial support was provided by National Science Foundation.  
Raymond Lau reports financial support was provided by US Department of Energy. If there are other authors, they declare that they have no known competing financial interests or personal relationships that could have appeared to influence the work reported in this paper.